Identification and separation of local and nonlocal optical nonlinear refraction effects: theory and experiment

Yuxiao Han (韩昱霄)[1], Bing Gu (顾 兵)[1,*], Shuai Zhang (张 帅)[1], Guanghao Rui (芮光浩)[1], Jun He (何 军)[2], and Yiping Cui (崔一平)[1]

[1]*Advanced Photonics Center, Southeast University, Nanjing 210096, China*
[2]*School of Physics and Electronics, Central South University, Changsha 410012, China*
**Corresponding author: gubing@seu.edu.cn*

Received December 27, 2018; accepted March 8, 2019; posted online May 31, 2019

Understanding the nonlinear optical effect of novel materials plays a crucial role in the fields of photonics and optoelectronics. Herein, we theoretically and experimentally investigate the simultaneous presence of third-order locally refractive nonlinearity and thermally induced nonlocal nonlinearity saturation. We present analytical expressions for the closed-aperture Z-scan trace and the number of spatial self-phase modulation (SSPM) rings, which allows one to unambiguously and conveniently separate the contributions of local and nonlocal nonlinear refraction in the case that both effects occur simultaneously. As a test, we study both the local and thermally induced nonlocal nonlinear refraction in fullerene/toluene solution by performing continuous-wave Z-scan and SSPM measurements at two different wavelengths. This work enriches the understanding of the physical mechanism of the optical nonlinear refraction effect in solution dispersions of nanomaterials, which can be exploited for nonlinear photonic devices.

OCIS codes: 190.4420, 190.4870.
doi: 10.3788/COL201917.061901.

In the past few decades, research efforts have been focused on novel materials, their nonlinear optical effects, and technological applications[1]. Among these materials, nanomaterial dispersions, such as graphene sheets[2], layered transition metal dichalcogenides[3], MoS_2 nanoflake[4,5], topological insulator Bi_2Te_3[6], and black phosphorus[7], have attracted extensive interest due to their broadband nonlinear optical response, chemical and thermal stabilities, and relatively low production cost. At the same time, the underlying mechanisms of the optical nonlinearities in nanomaterial dispersions, including purely coherent light scattering[2], third-order nonlinear refraction[3], and saturable absorption[8,9], have been investigated, although the understanding of these mechanisms is still incomplete[10].

Depending on the spatial distribution of nonlinear optical response relative to the optical intensity, optical nonlinearity can be categorized as local or nonlocal[11,12]. For the well-known local nonlinearity, the nonlinear optical response follows the intensity distribution. For the weakly (or highly) nonlocal nonlinearity, however, the nonlinear optical response is narrower (or wider) than the intensity distribution. As an example of local nonlinearity, third-order nonlinear refraction mainly arises from electrostriction, population redistribution, and electronic nonlinearity[10]. Generally, the physical mechanisms of nonlocal nonlinearities are thermally induced nonlinearity[13,14] and orientational optical nonlinearities in nematic liquid crystals[15]. In addition, the nonlocal nonlinear response can also be induced by atoms[11], charge carriers[16], etc. Recently, nonlocal nonlinearity has been exploited in a variety of technological applications, including solitons in nonlocal nonlinear media[17], far-field spatial self-phase modulation (SSPM) patterns by a thin nonlocal nonlinear medium[12,18], and the modified Z-scan theory for characterizing nonlocal nonlinearity[19,20].

To quantitatively appraise the optical nonlinearity of a material, researchers developed several nonlinear optical characterizing techniques, such as Z-scan[21], SSPM[22], and optical Kerr gate[23]. For example, investigations have reported on the nonlinear refractive index of nanomaterial dispersion in the SSPM experiments[24,25]. Moreover, the experimental observations have revealed that many materials exhibit more than one nonlinear optical process concurrently under the excitation of an intense laser beam, such as the concurrence of third- and fifth-order optical nonlinearities[26], two-photon-induced excited-state nonlinearities[27], and two simultaneous nonlocal nonlinear optical effects[28]. To fully exploit the material for potential application in nonlinear photonics devices, it is highly desirable to identify the physical mechanisms, separate their contributions, and determine the photophysical parameters when more than one nonlinear optical effect is simultaneously present.

In this work, using a fullerene/toluene solution as a test sample, we theoretically and experimentally investigate the simultaneous occurrence of local and thermally induced nonlocal nonlinear refraction. The analytical expressions for both the closed-aperture (CA) Z-scan trace and the power-dependent SSPM ring number allow one to unambiguously and conveniently separate the contributions of local and nonlocal nonlinear refraction in the case that both effects occur simultaneously. To verify our theory, we experimentally investigate the simultaneous

local and thermally induced nonlocal nonlinearities in a fullerene/toluene solution by performing continuous-wave (CW) Z scans and SSPM measurements at two different wavelengths.

Assuming that a CW laser beam with a Gaussian spatial profile is incident normally onto the absorbing solution at room temperature, there is a temperature increment in the solution, owing to absorption of the laser energy by the solution. To quantitatively determine the temperature variation in the material, we simulate the temperature distribution at the air–liquid interface with the typical parameters of the fullerene/toluene solution at 532 nm[29], by taking into account both thermal conduction and thermal convection. In the simulation, we consider radiative beams in absorbing media, heat transfer in fluids, and laminar flow, obtaining numerical solutions of nonisothermal flow under the condition of multi-physics coupling[30]. For example, the insert of Fig. 1 shows the distributions of the temperature variation for three laser irradiation powers P. Clearly, the temperature rises as the irradiation power increases. The maximum variation of the temperature is located at the center of the laser irradiation. Moreover, the temperature distributions maintain circular symmetry in the transverse plane. Interestingly, the temperature variation extends beyond the irradiation beam distribution due to the heat dissipation and exhibits highly nonlocal behavior. Figure 1 presents the power dependence of the maximum value of the temperature variation $\Delta T_{\max}$. It is shown that the value of $\Delta T_{\max}$ increases as the irradiation power P increases. However, this power-dependent $\Delta T_{\max}$ deviates from linearity, and a saturation trend occurs at relatively high irradiation power.

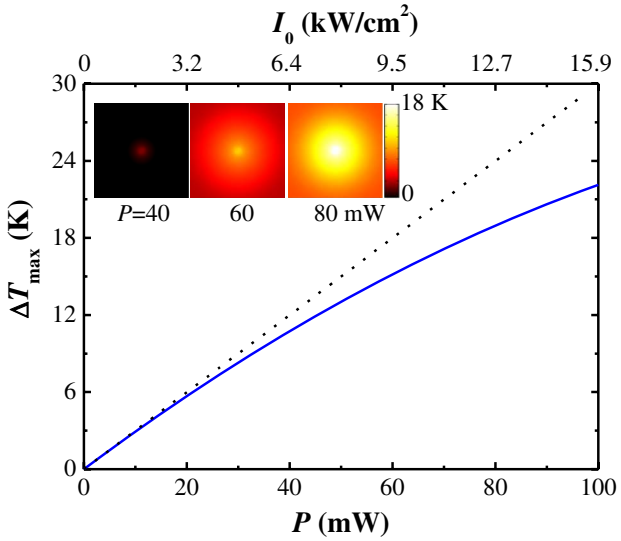

Fig. 1. Power (or intensity) dependence of the maximum value of the temperature variation in the light-absorbing liquid. The dashed line is a guide for the eyes. The insert is the patterns of the temperature variation under the irradiation of three powers.

The temperature increment in the solution induces a change in the refractive index by $\Delta n = (\mathrm{d}n/\mathrm{d}T) \cdot \Delta T$, where $\mathrm{d}n/\mathrm{d}T$ is the thermo-optical coefficient of the solution. Considering the saturation of thermally induced nonlocal nonlinearity (see Fig. 1), we model the change in the refractive index Δn as

$$\Delta n(r, z; u) = \frac{\mathrm{d}n}{\mathrm{d}T} \frac{\alpha_0 P}{2\pi K(1 + P/P_S)} \frac{\exp\left[-ur^2/\omega^2(z)\right]}{(1 + x^2)^{u/2}}. \quad (1)$$

Here, α_0 is the linear absorption coefficient of the solution. K is the thermal conductivity. P_S is the saturation power. The irradiation power P and the intensity $I(r, z)$ are related through the formula $P = 2\pi \int_0^\infty I(r, z) r \mathrm{d}r$, where $I(r, z) = [I_0/(1 + x^2)] \cdot \exp[-2r^2/\omega^2(z)]$, $\omega^2(z) = \omega_0^2(1 + x^2)$, $x = z/z_0$, $z_0 = k\omega_0^2/2$, $k = 2\pi/\lambda$, I_0 is the on-axis peak intensity at the focus, λ is the laser wavelength, and ω_0 is the waist radius of the Gaussian beam. The laser power P and the intensity I_0 are related through the formula $I_0 = 2P/(\pi\omega_0^2)$. The parameter u is the order of nonlocality and can be any real positive number[18]. Note that one can get $\Delta n(r, z; u) \propto \exp(-ur^2/\omega^2)/(1 + x^2)^{u/2}$ from Eq. (1), which is in agreement with the reported ones[18]. For the special case of unsaturated nonlocal nonlinearity (i.e., $P_S \to \infty$), the peak change in the refractive index $\Delta n(0, 0; u)$ is consistent with the one reported previously[31].

Under the excitation of the CW laser beam, in general, the light-absorbing solution exhibits local and nonlocal nonlinear refraction simultaneously. Under the thin-sample approximation and the slowly varying envelope approximation, the equations describing the propagation of the optical field within the sample are governed by

$$\frac{\mathrm{d}\Delta\phi(r, z)}{\mathrm{d}z'} = kn_2 I(r, z) + k\Delta n(r, z; u), \quad (2)$$

$$\frac{\mathrm{d}I(r, z)}{\mathrm{d}z'} = -\alpha_0 I(r, z), \quad (3)$$

where z' is the propagation distance inside the sample, and n_2 is the third-order nonlinear refractive index. It is emphasized that the saturation effect in the analysis arises from the thermally induced nonlocal nonlinearity instead of the local nonlinearity, which is demonstrated by the following experiments (see Fig. 2).

By combining Eqs. (1)–(3), the complex electric field at the exit plane of the sample is given by

$$E_e(r, z) = E(r, z) e^{-\alpha_0 L/2} \exp[i\Delta\phi(r, z) + i\Delta\phi'(r, z; u)], \quad (4)$$

where

$$\Delta\phi(r, z) = \frac{\Phi_2}{1 + x^2} \exp\left[-\frac{2r^2}{\omega^2(z)}\right], \quad (5)$$

$$\Delta\phi'(r,z;u)=\frac{\Phi_2'}{(1+x^2)^{u/2}}\exp\left[-\frac{ur^2}{\omega^2(z)}\right]. \tag{6}$$

Here, $\Phi_2=2kn_2L_{\rm eff}P/(\pi\omega_0^2)$ and $\Phi_2'\simeq\frac{{\rm d}n}{{\rm d}T}\frac{P}{1+P/P_S}\frac{k\alpha_0L_{\rm eff}}{2\pi K}$ are, respectively, the on-axis peak phase shifts due to the local and nonlocal refractive nonlinearities, which are proportional to the effective sample length $L_{\rm eff}=(1-e^{-\alpha_0L})/\alpha_0$. L is the sample physical length, and i is the imaginary number.

To characterize the optical nonlinearities of a material, the single-beam Z-scan technique is extensively adopted due to its experimental simplicity and high sensitivity[21]. Based on the Gaussian decomposition method[21,32], the complex electric field at the aperture plane can be easily obtained. Under the far-field approximation, we obtain the normalized power transmittance for the thin sample with both the local and nonlocal refractive nonlinearities as

$$T(x,s)=\frac{1}{s}\left[1-\sum_{m,m'=0}^{\infty}\sum_{v,v'=0}^{m,m'}F_{mm'}(1-s)^{\lambda_{mm'}}\cos\psi_{mm'}\right] \tag{7}$$

with

$$F_{mm'}=\frac{\Phi_2^{v+v'}\Phi_2'^{m+m'-v-v'}}{v!v'!(m-v)!(m'-v')!(C_{mv}+C_{m'v'}+1)(x^2+1)^{C_{mv}+C_{m'v'}}}, \tag{8}$$

$$\lambda_{mm'}=\frac{(C_{mv}+C_{m'v'}+1)(x^2+1)[x^2+(2C_{mv}+1)(2C_{m'v'}+1)]}{[x^2+(2C_{mv}+1)^2][(x^2+(2C_{m'v'}+1)^2]}, \tag{9}$$

$$\psi_{mm'}=\frac{\pi}{2}(m-m')-\frac{2(C_{mv}-C_{m'v'})(C_{mv}+C_{m'v'}+1)x(x^2+1)\ln(1-s)}{[x^2+(2C_{mv}+1)^2][(x^2+(2C_{m'v'}+1)^2]}, \tag{10}$$

$$C_{mv}=um/2-uv/2+v. \tag{11}$$

Here, s is the linear transmittance of the far-field aperture. In the special case that the sample only exhibits the local nonlinearity (i.e., $\Phi_2\neq0$ and $\Phi_2'=0$), Eq. (7) degenerates into the one we reported previously[32].

Alternatively, the light–matter interaction changes the space-dependent refractive index and affects the propagation behavior of the beam itself, resulting in a far-field intensity pattern of concentric diffraction rings. From the self-diffraction intensity pattern, one can visually estimate the nonlinear refractive index of material[22]. When the sample is located at the beam waist, the transverse additional phase shift induced on the exit plane of the sample can be expressed as[3]

$$\Delta\phi(r)=kn_0\int_0^{L_{\rm eff}}[n_2I(r,z)+\Delta n(r,z;u)]{\rm d}z, \tag{12}$$

where n_0 is the linear refractive index of the sample. Thus, the transverse phase shift leads to SSPM behavior. The electric fields on two different r points propagating on the far-field observation screen can interfere, giving rise to the appearance of self-diffraction patterns with the multiple concentric ring structures.

Based on Kirchhoff's diffraction principle under the cylindrical symmetry, we determine the intensity distribution in the observational plane by

$$I(r_a,d)=\frac{I_0k^2}{d^2}\left|\int_0^{+\infty}r_1J_0\left(\frac{kr_ar_1}{d}\right)\exp\left(-\frac{2r_1^2}{\omega_0^2}\right)\times\exp[-i(\phi_D+\phi_{\rm NL}+\phi'_{\rm NL})]{\rm d}r_1\right|^2 \tag{13}$$

with $\phi_D=-kr_1^2/(2d)$, $\phi_{\rm NL}=\Phi_2\exp(-2r_1^2/\omega_0^2)$, and $\phi'_{\rm NL}\simeq\Phi_2'\exp(-ur_1^2/\omega_0^2)$. Here, r_a is the radial position on the far-field observational plane, which is at a distance of d from the focal point. $J_0(\cdot)$ is the zero-order Bessel function of the first kind.

Quantitatively, the total number of self-diffraction rings N can be estimated from the relation $\Delta\phi(0)=2\pi N$[22]. From Eq. (12), we get

$$N=\frac{2n_0L_{\rm eff}P}{\lambda}\left[\frac{n_2}{\pi\omega_0^2}+\frac{{\rm d}n}{{\rm d}T}\frac{\alpha_0}{4\pi K(1+P/P_S)}\right]. \tag{14}$$

Equation (14) predicts that the number of self-diffraction rings is a monotonically nonlinear increasing function of the incident power. It is emphasized that this saturable behavior has been experimentally observed[4,22,33], although the corresponding interpretation is usually neglected, and the underlying mechanism cannot be completely explained. For the sample exhibiting the local nonlinear refraction only (i.e., ${\rm d}n/{\rm d}T\approx0$), Eq. (14) gives the linear relation between N and P (or I), which has been reported previously[2,6].

To verify our theory, we investigate the optical nonlinear refraction of the fullerene/toluene solution with a low concentration of 100 mg/L. The linear absorption coefficients of the solution are measured to be $\alpha_0=0.037$ and $0.213\ {\rm cm}^{-1}$ at 671 and 532 nm, respectively. It is expected that the huge difference of α_0 at 671 and 532 nm gives us the possibility to identify different optical nonlinear refraction effects.

In the Z-scan measurements, the CW laser beams with nearly Gaussian spatial profiles at 671 and 532 nm were focused by a lens with a focal length of 200 mm, producing

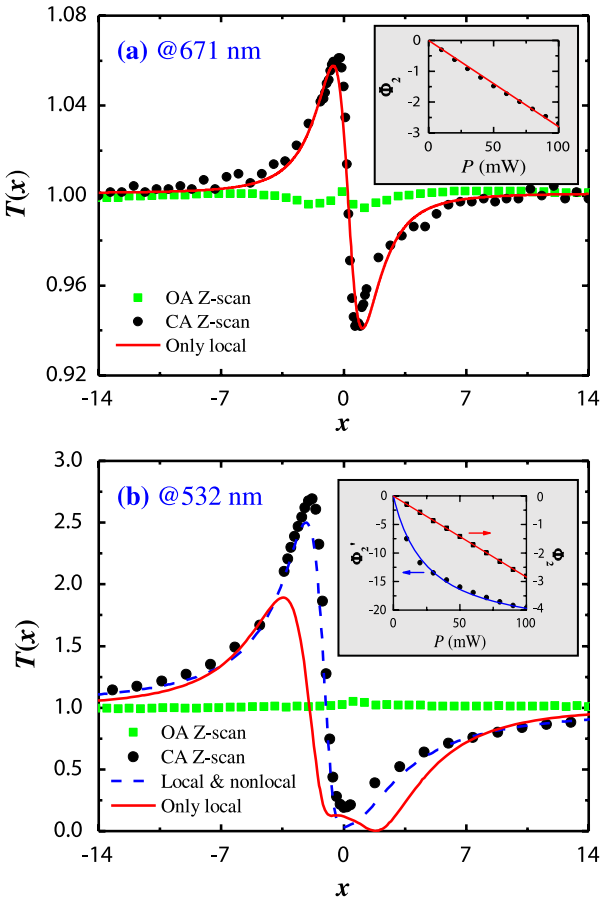

Fig. 2. Examples of CA Z-scan traces for fullerene/toluene solution with the same excitation power of 10 mW at the wavelengths of (a) 671 nm and (b) 532 nm, respectively. The scatters are the experimental data, while the solid (or dashed) lines are the theoretical fits by the Z-scan theory on local without (or with) nonlocal refractive nonlinearities described in the text. The inserts of (a) and (b) are the measured nonlinear phase shifts versus the excitation power P.

the beam waist of $\omega_0 \approx 20$ μm (the corresponding Rayleigh ranges z_0 are estimated to be 1.87 and 2.36 mm at 671 and 532 nm, respectively). The fullerene/toluene solution was contained in 2-mm-thick quartz cells. Although the sample thickness L is comparable to the Rayleigh range z_0, the thin-sample approximation for standard Z-scan analysis is still valid since Chapple *et al.*[34] demonstrated that the sample thickness could be extended to $3.1z_0$. To carry out the Z-scan experiments, the sample was scanned across the focus along the optical axis using a computer-controlled translation stage, while the transmitted powers in the presence or absence of the far-field aperture were recorded by a detector as a function of the sample position z, obtaining the CA and open-aperture (OA) Z scans, respectively. For the CA Z scans, the linear transmittances of the far-field aperture were, respectively, measured to be 0.2 and 0.3 at 671 and 532 nm.

To identify the underlying mechanisms of the observed optical nonlinearities, we performed the Z-scan measurements at different levels of incident powers. At both 671 and 532 nm, it is shown that the signals of the CA Z scans are much larger than those of the OA Z scans (e.g., see Fig. 2), and all CA Z-scan traces have the characteristic of peak-to-valley configuration, indicating that the fullerene/toluene solution has insignificant nonlinear absorption and negative nonlinear refraction. In addition, we also carried out the Z scans on pure toluene, and no Z-scan signal was observed, validating that the pure refractive nonlinearity originates from fullerene only.

It is well documented that reverse saturable absorption is a dominant mechanism (via a populated real singlet with the lifetime of $\tau_S \leq 1$ ns and triplet states with the lifetime of $\tau_T \geq 40$ μs) in the nonlinear absorption process of fullerene at visible wavelengths[35,36]. This reverse saturable absorption effect has been observed in fullerene with the pulsed laser[35,36] and the chopped laser[37]. Under the excitation of a CW laser beam, however, reverse saturable absorption becomes insignificant to the overall nonlinear absorption process, as it is too slow to respond. That is why we did not detect the nonlinear absorption of fullerene/toluene solution in our experimental conditions.

Inasmuch as all the measured Z scans at different P are similar in configuration, as an example, Figs. 2(a) and 2(b) show the Z-scan traces for the fullerene/toluene solution with the same excitation power of 10 mW at 671 and 532 nm, respectively. Firstly, under the assumption that the solution only has local nonlinearity, we use Eq. (7) with $\Phi_2' = 0$ to fit the Z-scan traces. At 671 nm, the fitting result of $\Phi_2 = -0.31$ [see the solid line in Fig. 2(a)] is in good agreement with the experimental data, suggesting that the sample should have local nonlinear refraction, whereas the nonlocal nonlinear refraction is ignorable. Furthermore, the obtained Φ_2 value is proportional to the incident power P [see the insert in Fig. 2(a)], indicating that the observed local nonlinearity is a pure third-order nonlinear refraction in nature. Accordingly, the third-order nonlinear refractive index of the fullerene/toluene solution at 671 nm is measured to be $n_2 = -(9.8 \pm 0.7)$ cm^2/GW. At 532 nm, however, the Z-scan theory on the local nonlinear refraction does not fit the Z-scan experimental result well [see the solid line in Fig. 2(b)]. One can infer that the sample should have other nonlinear process additions to the local nonlinearity. By the best fitting of Eq. (7) to the Z-scan experimental data with the known parameters of $z_0 = 2.36$ mm and $s = 0.3$ at 532 nm, we obtain $\Phi_2 = -0.29$, $\Phi_2' = -7.50$, and $u = 0.56$. Apparently, nonlocal nonlinear refraction is much stronger than local nonlinear refraction. Furthermore, the observed nonlocal nonlinear refraction arises from the thermally induced nonlinearity because of the strong linear absorption at 532 nm. The dashed line in Fig. 2(b) indicates that the Z-scan theory for the sample with both the local and nonlocal refractive nonlinearities correctly describes the CA Z-scan experimental results, although there are some differences between the theoretical fit and the experimental results. The main reason is that the Z-scan theory adopts the thin-sample approximation, while the sample thickness is comparable to the

Rayleigh range in the Z-scan experiments. The insert of Fig. 2(b) shows that the measured value of Φ_2 is proportional to the incident power P, whereas the Φ_2' value deviates from linearity, and a saturation trend at relatively high incident power occurs. Moreover, all of the CA Z-scan traces at 532 nm measured at the other incident powers can also be well reproduced by the presented Z-scan theory [see Eq. (7)].

In the SSPM experiments, a CW laser beam at 532 nm was focused by a lens with a focal length of 125 mm, producing the beam waist at the focus of $\omega_0 \approx 20$ μm. The SSPM experimental setup is similar to the one reported previously[3]. The solution was contained in quartz cells with a pathlength of 10 mm. The front surface of the sample was placed at the focal plane of the focused beam. A black screen was put 520 mm away from the sample. Note that the laser beam propagating vertically is incident normally onto the sample lying horizontally in order to eliminate gravity-induced distortion of self-diffraction rings[38].

As shown the top row of Fig. 3(a), owing to SSPM happening in the fullerene/toluene solution, the far-field intensity patterns with the multiple concentric ring structures were experimentally observed at different levels of incident powers P. The observed self-diffraction ring patterns have the following characteristics: (i) the pattern presents a central bright spot; (ii) the outmost ring has the higher intensity compared with the inner ring; and (iii) as the value of P increases, the number of bright diffraction rings around the bright spot increases, and more light power is diffracted into the outer rings. Using Eq. (13) with the known experimental parameters of $d = 520$ mm, $L_{\text{eff}} = 9.0$ mm, $\omega_0 = 20$ μm, and the thermal-optical parameters of $\mathrm{d}n/\mathrm{d}T = 5.3 \times 10^{-4}$ K^{-1} and $K = 0.127$ W/(m · K)[29], we estimate $n_2 = -9.82$ cm^2/GW, $P_S = 55.5$ mW, and $u \approx 0.6$. Accordingly, the simulated far-field self-diffraction ring patterns are displayed in the bottom row of Fig. 3(a). Clearly, the theoretical simulations are consistent with the experimental observations, indicating that our theoretical analysis is reasonable and could gain an insight on the underlying mechanisms for the observed SSPM effect.

Figure 3(b) illustrates the number of rings N (excluding the center bright spot) as a function of excitation power P or laser intensity I_0 at 532 nm. It is shown that the number of diffraction rings increases nearly linearly with the incident power. At relatively high power, however, the saturation effect occurs, as shown in Fig. 3(b). It is noteworthy that this saturation tendency is usually neglected and regarded as a linear relation roughly excluding the saturable signal[4,33]. The observed saturable behavior can be understood as follows. Under our experiment conditions, the power-dependent temperature increment in the solution exhibits the saturable effect (see Fig. 1). Subsequently, the saturation of thermally induced nonlocal nonlinearity occurs at relatively high incident power, resulting in the saturation of the number of diffraction rings [see Fig. 3(b)]. On the other hand, as shown in

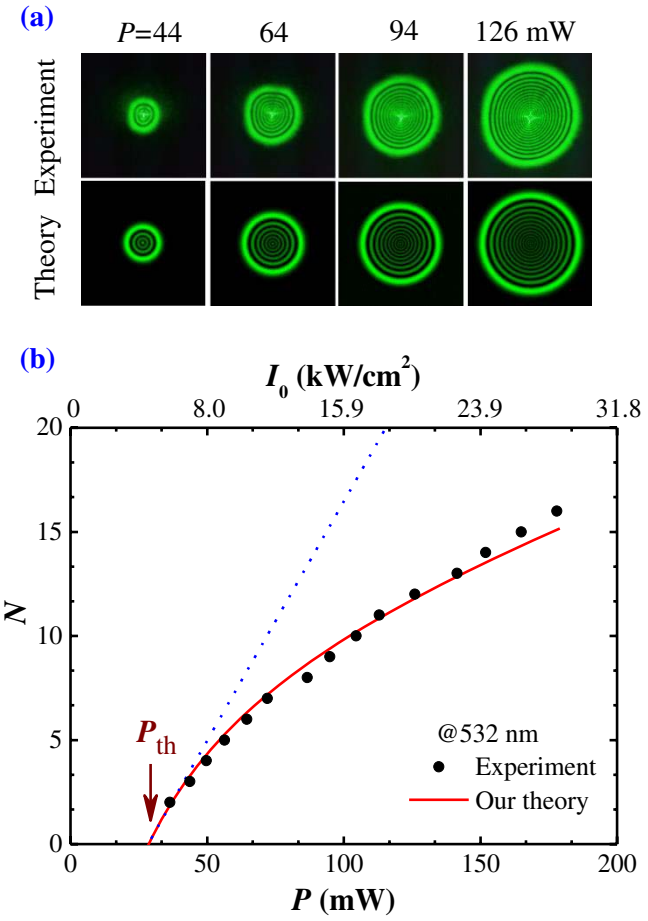

Fig. 3. (a) Experimentally observed and theoretically simulated far-field intensity patterns for fullerene/toluene solution at the wavelength of 532 nm with four different incident powers. (b) The number of self-diffraction rings versus the incident power or the intensity. The circles are the experimental data, while the solid line is the theoretical fit by Eq. (14) described in the text. The dashed line is a guide for the eyes.

Fig. 3(b), the power (or intensity) threshold for observing the SSPM patterns in the fullerene/toluene solution is estimated to be 28.9 mW (or 4.6 kW/cm^2). This threshold behavior has been observed in solution dispersions of graphene sheets[2], separate MoS_2 flakes[4], and $MoSe_2$ nano-sheets[33]. If the power threshold occurs in the SSPM pattern, one should modify P with $P - P_{\text{th}}$ in Eq. (14). With the known experimental parameters, the best fit [see the solid line in Fig. 3(b)] gives $n_2 = -(10.9 \pm 0.8)$ cm^2/GW and $P_S = 50.5$ mW, which are close to the ones obtained by the far-field intensity patterns.

It is noteworthy that we did not observe the SSPM diffraction rings at 671 nm under similar experimental conditions at 532 nm. This difference is anticipated for the following reasons: (i) the intrinsic third-order local nonlinear refraction at 671 nm is close to that at 532 nm, supported by the Z-scan results; (ii) the nonlocal nonlinear refraction effect is negligible at 671 nm, while this effect is very strong at 532 nm; and (iii) the resultant nonlinear effect of local and nonlocal nonlinearities at

532 nm, which contributes to the SSPM diffraction rings, is much larger than that at 671 nm.

In summary, we have theoretically and experimentally investigated a sample exhibiting both thermally induced nonlocal nonlinear refraction saturation and local nonlinear refraction. We have presented analytic theories for the Z-scan trace and the power-dependent SSPM ring number for straightforwardly and unambiguously characterizing the local and nonlocal nonlinear refraction simultaneously. Experimentally, we have identified and separated both the local and thermally induced nonlocal nonlinearities in fullerene/toluene solution by performing CW Z-scan and SSPM measurements at two different wavelengths. The presented work enriches the understanding of underlying mechanisms of optical nonlinearity in nanomaterials, which can be exploited for nonlinear photonic devices.

This work was supported by the National Natural Science Foundation of China (Nos. 11774055 and 11474052) and the Natural Science Foundation of Jiangsu Province (No. BK20171364).

References

1. G. S. He, L. S. Tan, Q. D. Zheng, and P. N. Prasad, Chem. Rev. **108**, 1245 (2008).
2. R. Wu, Y. Zhang, S. Yan, F. Bian, W. Wang, X. Bai, X. Lu, J. Zhao, and E. Wang, Nano Lett. **11**, 5159 (2011).
3. G. Wang, S. Zhang, X. Zhang, L. Zhang, Y. Cheng, D. Fox, H. Zhang, J. N. Coleman, W. J. Blau, and J. Wang, Photon. Res. **3**, A51 (2015).
4. Y. Wu, Q. Wu, F. Sun, C. Cheng, S. Meng, and J. Zhao, Proc. Natl. Acad. Sci. USA **112**, 11800 (2015).
5. S. Xiao, B. Lv, L. Wu, M. Zhu, J. He, and S. Tao, Opt. Express **23**, 5875 (2015).
6. B. Shi, L. Miao, Q. Wang, J. Du, P. Tang, J. Liu, C. Zhao, and S. Wen, Appl. Phys. Lett. **107**, 151101 (2015).
7. B. Guo, Chin. Opt. Lett. **16**, 020004 (2018).
8. F. Zhao, Y. Wang, Y. Wang, H. Wang, and Y. Cai, Chin. Opt. Lett. **15**, 101402 (2017).
9. R. K. Yadav, R. Sharma, J. Aneesh, P. Abhiramnath, and K. V. Adarsh, Opt. Lett. **41**, 2049 (2016).
10. D. N. Christodoulides, I. C. Khoo, G. J. Salamo, G. I. Stegeman, and E. W. Van Stryland, Adv. Opt. Photon. **2**, 60 (2010).
11. D. Suter and T. Blasberg, Phys. Rev. A **48**, 4583 (1993).
12. E. V. G. Ramirez, M. L. A. Carrasco, M. M. M. Otero, S. C. Cerda, and M. D. I. Castillo, Opt. Express **18**, 22067 (2010).
13. J. P. Gordon, R. C. C. Leite, R. S. Moore, S. P. S. Porto, and J. R. Whinnery, J. Appl. Phys. **36**, 3 (1965).
14. F. W. Dabby and J. R. Whinnery, Appl. Phys. Lett. **13**, 284 (1968).
15. I. C. Khoo, T. H. Liu, and P. Y. Yan, J. Opt. Soc. Am. B **4**, 115 (1987).
16. M. Segev, B. Crosignani, A. Yariv, and B. Fischer, Phys. Rev. Lett. **68**, 923 (1992).
17. G. Liang, W. Hong, and Q. Guo, Opt. Express **24**, 28784 (2016).
18. B. A. M. Irivas, M. L. A. Carrasco, M. M. M. Otero, R. R. García, and M. D. I. Castillo, Opt. Express **23**, 14036 (2015).
19. M. R. R. Vaziri, F. Hajiesmaeilbaigi, and M. H. Maleki, J. Opt. **15**, 025201 (2013).
20. M. R. R. Vaziri, Appl. Opt. **52**, 4843 (2013).
21. M. Sheik-Bahae, A. A. Said, and E. W. Van Stryland, Opt. Lett. **14**, 955 (1989).
22. S. D. Durbin, S. M. Arakelian, and Y. R. Shen, Opt. Lett. **6**, 411 (1981).
23. E. P. Ippen and C. V. Shank, Appl. Phys. Lett. **26**, 92 (1975).
24. G. Wang, S. Zhang, F. A. Umran, X. Cheng, N. Dong, D. Coghlan, Y. Cheng, L. Zhang, W. J. Blau, and J. Wang, Appl. Phys. Lett. **104**, 141909 (2014).
25. G. Wang, S. Higgins, K. Wang, D. Bennett, N. Milosavljevic, J. J. Magan, S. Zhang, X. Zhang, J. Wang, and W. J. Blau, Appl. Opt. **57**, E147 (2018).
26. A. A. Said, M. Sheik-Bahae, D. J. Hagan, T. H. Wei, J. Wang, J. Young, and E. W. Van Stryland, J. Opt. Soc. Am. B **9**, 405 (1992).
27. B. Gu, Y. Sun, and W. Ji, Opt. Express **16**, 17745 (2008).
28. B. A. M. Irivas, M. L. A. Carrasco, M. M. M. Otero, R. R. García, and M. D. I. Castillo, Opt. Express **24**, 13387 (2016).
29. M. Ahmed and T. Riffat, J. Mod. Opt. **51**, 1663 (2004).
30. E. B. Christiansen and G. E. Jensen, AIChE J. **15**, 504 (1969).
31. J. G. Tian, C. Zhang, G. Zhang, and J. Li, Appl. Opt. **32**, 6628 (1993).
32. B. Gu, J. Chen, Y. X. Fan, J. Ding, and H. T. Wang, J. Opt. Soc. Am. B **22**, 2651 (2005).
33. W. Wang, Y. Wu, Q. Wu, J. Hua, and J. Zhao, Sci. Rep. **6**, 22072 (2016).
34. P. B. Chapple, J. Staromlynska, and R. G. McDuff, J. Opt. Soc. Am. B **11**, 975 (1994).
35. C. Li, L. Zhang, R. Wang, Y. Song, and Y. Wang, J. Opt. Soc. Am. B **11**, 1356 (1994).
36. S. Couris, E. Koudoumas, A. A. Ruth, and S. Leach, J. Phys. B: At. Mol. Opt. Phys. **28**, 4537 (1995).
37. F. Z. Henari, S. MacNamara, O. Stevenson, J. Callaghan, D. Weldon, and W. J. Blau, Adv. Mater. **5**, 930 (1993).
38. W. Ji, W. Chen, S. Lim, J. Lin, and Z. Guo, Opt. Express **14**, 8958 (2006).